Second Pulse Current in Resistance Spot Welded TRIP Steel — Effects on the Microstructure and Mechanical Behavior

The second pulse current improved mechanical properties when the fusion zone microstructure consisted of a recrystallized structure of martensite

BY V. H. BALTAZAR HERNANDEZ, Y. OKITA, AND Y. ZHOU

ABSTRACT

Resistance spot welds (RSW) in transformation-induced plasticity (TRIP) steel sheets were locally postweld heat treated by applying a second pulse of current in the welding schedule. The evolution of the fusion zone (FZ) microstructure by optical and scanning electron microscopy, microhardness, and standardized quasi-static lap-shear tensile testing was investigated for all the pulse current conditions. The most important result of this study is that improved mechanical properties with desirable pullout failure mode is accomplished when the FZ microstructure consists of a recrystallized structure of martensite, which was achieved in the medium level of the second pulse current postweld heat treatment. Even though a considerable reduction in FZ hardness was observed at the lowest value of the second pulse current due to the presence of plate-like ferrite and tempered martensite structure, the failure mode and load-bearing capacity of the weldment was not improved significantly. At higher current levels of the second pulse condition, remelting occurred with consequent formation of a new weld nugget comprising columnar structure but larger nugget size giving mixed failure modes. The fusion zone microstructures and microhardness results correlated well with the simulated welding thermal history of the postweld local heat treatments.

Introduction

Continued developments in advanced high-strength steels (AHSS) have helped automobile engineers in manufacturing vehicles with lower weight, better fuel efficiency, and increased crashworthiness. Among all the advanced high-strength steels, viz. dual-phase (DP), transformation-induced plasticity (TRIP), complex phase (CP), and martensitic (M) steels, TRIP has been reported to be a good candidate to facilitate gauge reduction and attain an exceptional combination of strength and ductility (Ref. 1).

Resistance spot welding (RSW) is the most widely used welding process for manufacturing auto-body structures (Ref. 2) and is also established as the favored welding process for joining AHSS (Refs. 3, 4), i.e., TRIP steel. However, it has been stated that RSW of TRIP steels has issues of weldability problems due to the relatively higher alloying level in these steels (Ref. 5). Inconsistent interfacial failure (IF) or partial interfacial (PI) failure modes coupled with diminished mechanical performance are the most common problems encountered in resistance spot welded TRIP steel (Refs. 6, 7).

One way of modifying the performance of resistance welds in general is to alter the microstructure by applying a postweld heat treatment. A local postweld heat treatment can be accomplished by inducing a second current pulse just after the primary (or first) welding current pulse. Such a resistance spot welding practice has been denominated in different ways, e.g., two-pulse current (Ref. 8), second impulse or second pulse current (Ref. 9), or in-process temper (Ref. 10). A short cooling time is sometimes allowed for the molten material to solidify completely before commencing the postweld heat treatment.

Only limited efforts have been made to evaluate the mechanical properties of RSW-TRIP steel after postweld heat treatments (Refs. 5, 11). For instance, RSW-TRIP steel grades 600 and 800 MPa were in-situ tempered, and the response to tempering was evaluated through peel and hardness testing. Although the macrostructure and hardness were shown for different combinations of current and time, the correlation of microstructure evolution and temperature profiles to the lap-shear tensile behavior were not reported (Ref. 11). After welding TRIP590, cross-tension specimens were heat treated in an air (muffle) furnace for 3600 s (1 h) in the temperature range 300°–650°C. It was reported that even though the strength was improved after heat treatment at temperatures above 600°C, the influence of microstructural changes on the mechanical response was not clear due to the fact that the heat treatment was performed over the entire specimen (Ref. 12). Postweld heat treatments were applied to TRIP700 steel by means of two and three impulse current, and the cross-tension tensile failures were evaluated. It was observed that the failure mode changed from interfacial to pullout after extended welding time (three pulses); however, the final strength and detailed microstructure of the spot welded TRIP700 steel were not reported (Ref. 5).

In this work, a systematic study has been conducted on resistance spot welding of TRIP steel sheets by applying local postweld heat treatments through second impulse current in order to alter the fusion

KEYWORDS

Transformation-Induced Plasticity (TRIP) Steels
Resistance Spot Welding
Microstructure
Hardness
Second Pulse Current

V. H. BALTAZAR HERNANDEZ (vhbaltaz@uwaterloo.ca)*, Y. OKITA, and Y. ZHOU are with Centre for Advanced Materials Joining, University of Waterloo, Canada. BALTAZAR HERNANDEZ is also with Autonomous University of Zacatecas, Mexico, and Y. OKITA is also with JFE Steel Corp., Japan.*

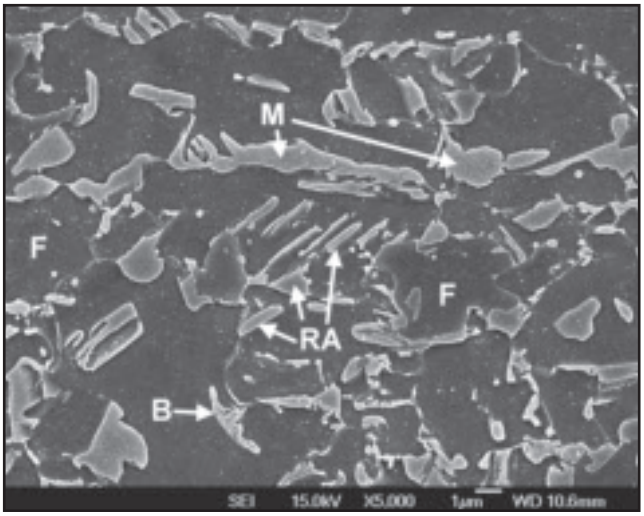

Fig. 1 — Base metal microstructure of TRIP steel showing the ferrite (F) matrix, the islands of martensite (M), retained austenite (RA), and bainite (B).

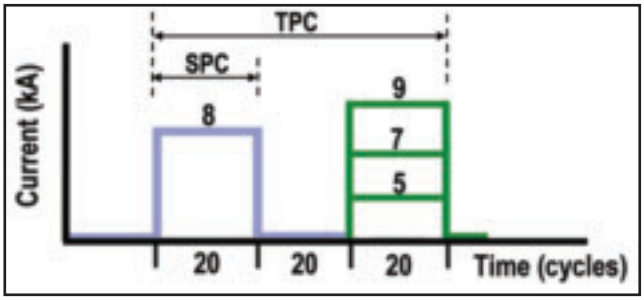

Fig. 2 — Schematic of resistance spot welding pulsing current schedules. Single-pulse current (SPC) and two-pulse current (TPC).

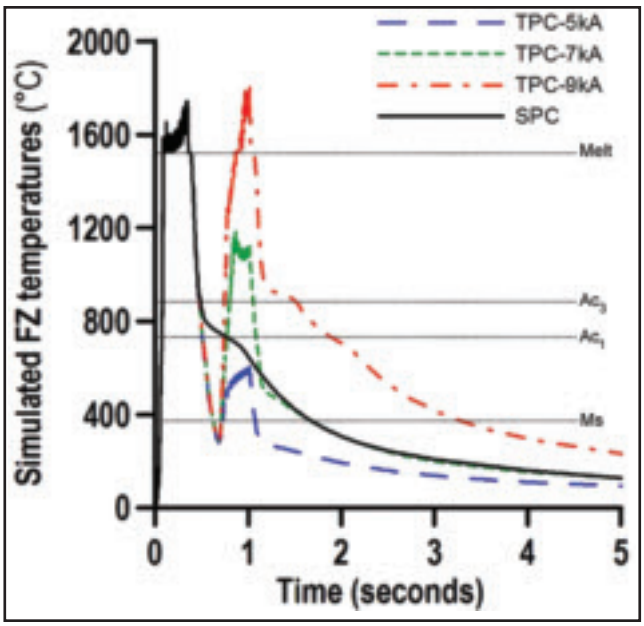

Fig. 3 — Simulated welding thermal cycles for single-pulse (SPC) and two-pulse current (TPC) conditions at different current levels.

zone microstructure and, consequently, the mechanical performance. In particular, the relationship has been established among the second impulse current, microstructural evolution occurring within the fusion zone, and lap-shear tensile behavior.

Experimental

TRIP steel with a nominal tensile strength of 800 MPa (TRIP800) was the starting material for this study. The TRIP steel used was in the form of 1.0-mm-thick sheet. The chemical composition of TRIP steel is listed in Table 1. It can be noted that Si content is relatively high, and this steel is also known as Si-alloyed TRIP steel (Ref. 13). The carbon equivalent of the TRIP steel used here was calculated by Yurioka's (Ref. 14) formula and is listed in Table 2. Transformation temperatures such as the martensite start temperature (M_s), and the critical transformation temperatures (Ac_1 and Ac_3) of the particular TRIP steel were calculated (Table 2) using the equations reported earlier (Ref. 15). The base metal (BM) microstructure of the TRIP steel is composed of the ferrite matrix (F) in dark along with varied fractions of bainite (B), martensite (M), and retained austenite (RA), as illustrated in Fig. 1. Using metallographic techniques, the volume fraction of the retained austenite was measured to be ~12%.

Resistance spot welds were conducted in a CenterLine Ltd. 250-kVA, single-phase AC resistance spot welding machine. It is a pedestal-type, pneumatically operated machine, with a Robotron™ constant current control and applied a frequency of 60 Hz. As per the Resistance Welding Manufacturing Alliance (RWMA) standards (Ref. 9), truncated Class 2 copper electrodes having a face diameter of 6.0 mm were used. A constant water flow rate of 4 L/min was maintained for cooling the electrodes. In order to minimize the dynamic behavior of electrode break-in and wear, a stabilization procedure was performed following the AWS standards (Ref. 16).

This steel was subjected to two different kinds of welding procedures in RSW as follows: In the first type of procedure, a conventional welding schedule was applied to heat, melt, and subsequently cool down the specimen. In the second version, after a conventional welding schedule (melting and cooling), a postweld heat treatment was carried out in the spot welding machine by reheating the specimen to a specific (aim) peak temperature followed by rapid cooling. The conventional welding schedule applied to TRIP steel consisted of a single-pulse current (SPC), and the postweld heat treatment condition was performed by a second pulse current at one of three different current levels. The schematic illustration of the welding schedules of SPC and two-

Table 1 — Chemical Composition of TRIP Steel (wt-%)

C	Mn	P	Si	Cu	Ni	Cr	Mo	Al
0.18	1.63	0.01	1.61	0.02	0.016	0.02	0.01	0.03

Table 2 — Carbon Equivalent and Calculated Transition Temperatures of TRIP Steel

	Temperature (°C)			
CE_Y	Melting Temperature	Ac_3	Ac_1	M_s
0.527	1540	915	747	380

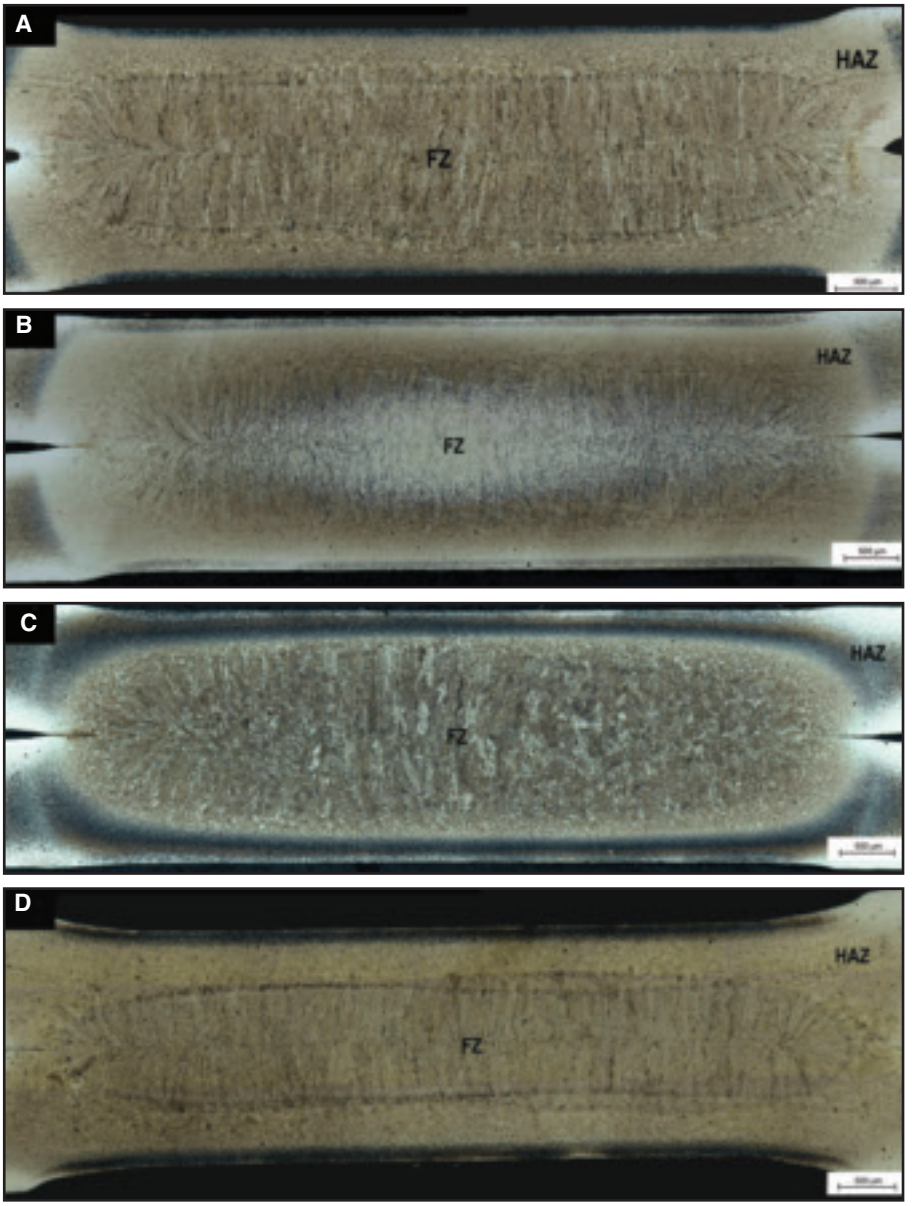

Fig. 4 — Cross-section macrostructures of TRIP steel resistance spot welded with the following: A — single-pulse current (8 kA), and second-pulse current of B — 5 kA; C — 7 kA; D — 9 kA.

pulse current (TPC) is depicted in Fig. 2. In addition, the complete welding schedule with the technical parameters used in the study is listed in Table 3. A range of current levels between 5 and 9 kA with an increment of 2 kA were applied in the second pulse schedule/cycle. A cooling time of 20 cycles was employed between the applied pulses.

The weld nugget size was evaluated by metallographic sample preparation techniques. Several specimens from each batch of nominally identical weldments were sectioned across the weldment, covering all the weld zones (FZ and HAZ) along with the BM. Fifty percent of each specimen group was sectioned parallel to the prior sheet rolling direction and the remaining half perpendicular to it. The specimens were mounted, ground, and polished followed by etching. In order to fully reveal and delineate the weld nugget boundary (i.e., weld interface), the mounted specimens were immersed in Vilella's solution (Ref. 17) for periods of 6 to 8 s. A minimum of four specimens from each group were analyzed for measuring the width of the nugget and average values are presented.

With the purpose of carrying on observations through optical microscopy, the specimens were chemically etched by employing Vilella's solution for 3 to 5 s then followed by nital solution for 3 to 5 s. This etching procedure permitted analyzing the FZ microstructure; particularly for delineating the prior austenite grain boundaries and the solidification structure observed by optical microscopy. On the other hand, after etching the samples with 1% nital solution by immersion for 10 s, the microstructure was analyzed by scanning electron microscopy (SEM). Vickers microhardness (HV) measurements were performed under a load of 200 g with a dwell time of 15 s and maintaining a distance of 200 μm between consecutive indentations.

Quasi-static lap-shear tensile tests were conducted with an Instron 4206 universal testing machine. Coupons were used with dimensions (105 × 45 mm) based on AWS standards (Ref. 16). A constant cross-head velocity was maintained at 10 mm/min. Shims were used for avoiding extraneous bending moments during the tensile tests.

Due to the technical difficulties in obtaining experimental weld thermal history in resistance spot welding (Ref. 18), and in order to further understand the changes in microstructure occurring due to the application of varied second pulse current procedures, numerical simulations of single-pulse and two-pulse current conditions were conducted to estimate the weld and postweld thermal history within the nugget. The weld thermal history within the fusion zone (FZ) was estimated through numerical simulation. A commercial finite element software coupled with electrical-thermal-mechanical analysis, Quick Spot by Research Center of Computational Mechanics, Inc., Japan, was used to run the thermal simulation (Ref. 19). A two-dimensional axisymmetric elastic-plastic model with a total number of 852 nodes was designed with a mesh density of 64 elements per mm^2 within the FZ. Material properties (i.e., thermal conductivity, specific heat, yield strength, and electrical conductivity) were taken into account and assumed to be temperature dependent. The welding parameters used in these simulations were kept similar to

Table 3 — Resistance Spot Welding Parameters

Welding current (kA)	Second-pulse current (kA)	Force (kN)	Squeeze time (cycles)	Hold time (cycles)	Cooling time between pulses (cycles)
8	5, 7, 9	4.5	25	5	20

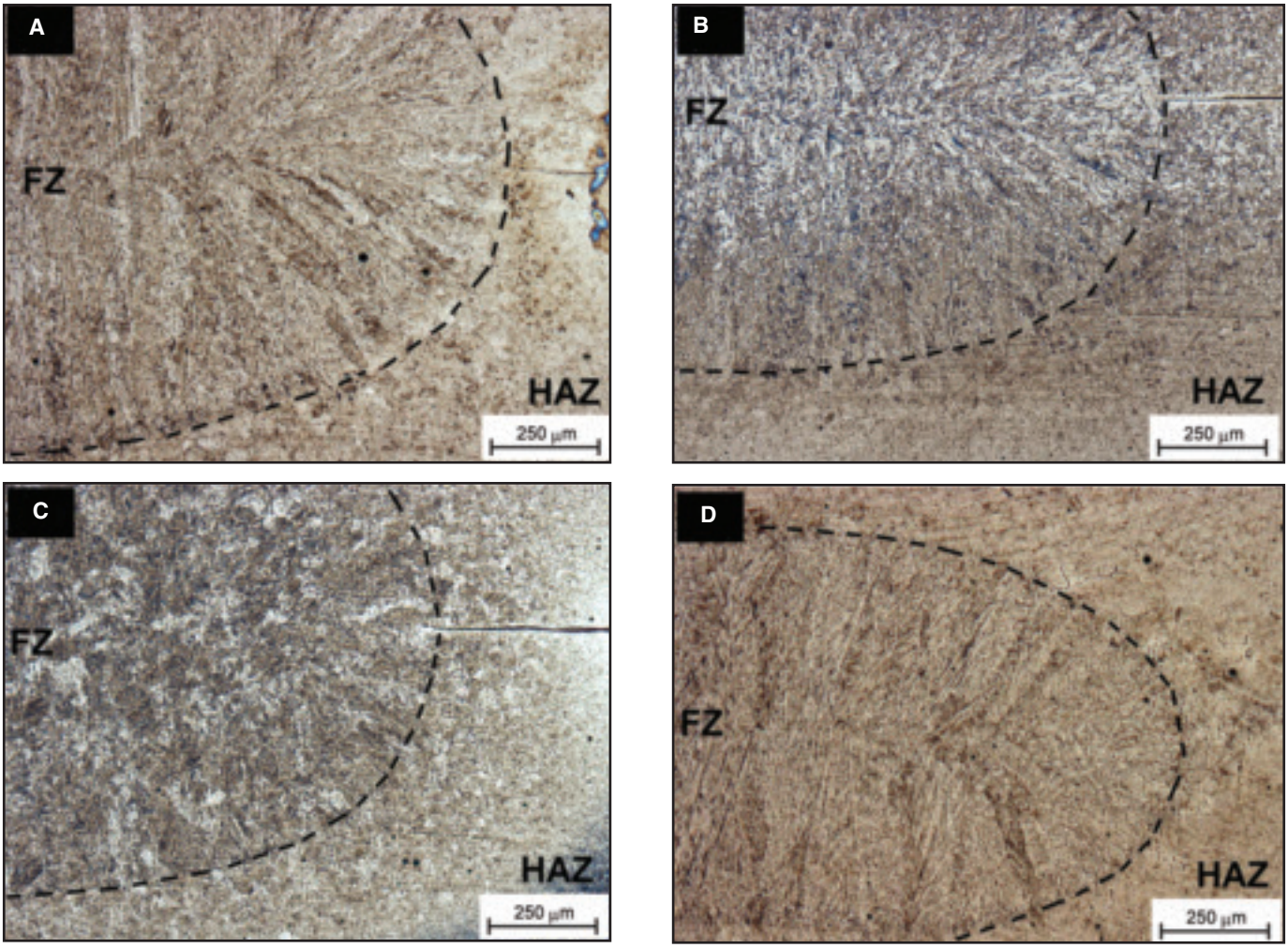

Fig. 5 — Optical images illustrating the FZ microstructure in specimens subjected to the following: A —Single-pulse current (8 kA), and second-pulse current of B — 5 kA; C — 7 kA; D — 9 kA.

those established during the welding experiments. The estimated peak temperatures of the fusion zone were obtained through nodal analysis.

The simulated thermal curves of all the four conditions studied (i.e., SPC and TPC at 5, 7, and 9 kA) are shown in Fig. 3. It should be noted that the first current impulse of the TPC specimens overlaps with the SPC curve until the former reaches the cooling temperature of approximately 800°C, and below this temperature the SPC and TPC curves separate. This is due to the fact that the electrodes are removed from the specimen surface after 5 cycles of hold time for the case of SPC, whereas a longer time of cooling (i.e., 20 cycles with the full electrode force applied as indicated by Table 3) was experienced by the TPC specimens before implementing the second impulse current. Based on the previously mentioned cooling procedure, all TPC specimens achieved an approximate temperature of 285°C upon cooling just before performing the second impulse current.

Results and Discussion

Weld Nugget

The weld cross sections of the TRIP steel welds showing various distinct regions of the weldment viz. fusion zone, heat-affected zone (HAZ), and base metal are provided in Fig. 4 for SPC and TPC specimens. The FZ optical micrographs obtained from the weld nuggets for SPC welding condition and TPC welds are illustrated in Fig. 5. It should be noted that the edge of the weld nugget (weld interface) has been delineated by dashed lines — Fig. 5.

The macrostructure of the SPC specimen in Fig. 4A shows the periphery of the weld nugget clearly delineated whereas the FZ microstructure in Fig. 5A illustrates elongated columnar grain growth that meets at the centerline of the nugget from the top and bottom weld interfaces. It is noteworthy that the solidification structure (primary structure) is partially observed along with the postsolidification weld microstructure (solid-state transformation). The elongated columnar growth seemed influenced by the solidification path of the primary structure. In fact, it has been stated that postsolidification weld microstructures are developed in the grain interior and/or along the grain boundaries of the primary structure (Ref. 20). Thus, the elongated columnar growth observed in Fig. 5A should be associated to prior austenite grain boundaries.

The representative macrostructure of the TPC 5-kA specimens shown in Fig. 4B illustrates distinctive macrostructural changes with respect to that of the SPC condition; for example, the periphery of the weld nugget seemed partially wiped out due to the effect of the postweld heat treatment (TPC). Thus, the prior weld nugget appearance partially disappeared; instead, a brighter region evolved at the center of the nugget (Fig. 4B) due to the effect of heat distribution during the second impulse current and formation of fine needle- and/or plate-like morphologies predominantly located at the centerline of the weld nugget as observed in Fig. 5B. Temperatures below Ac_1 were developed

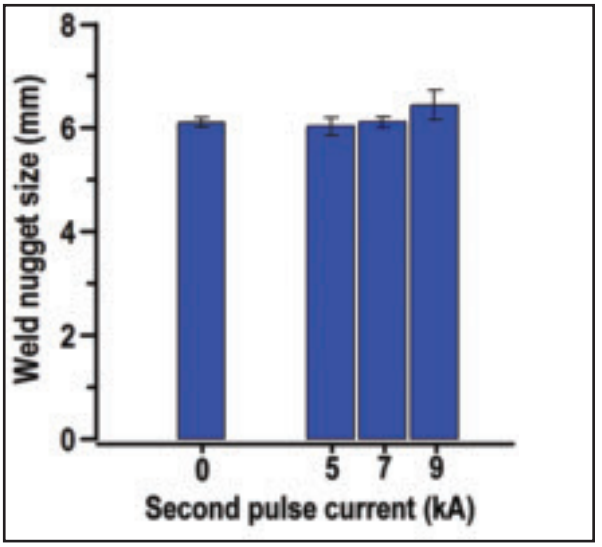

Fig. 6 — Weld nugget size by cross-sectioned measurements using metallographic techniques.

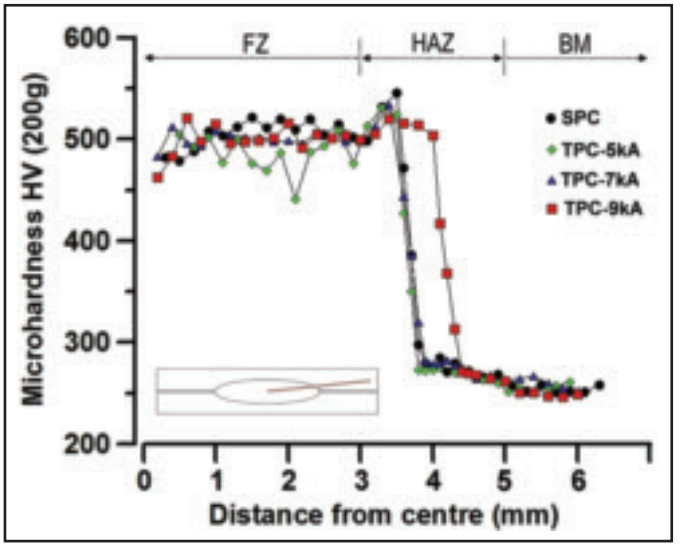

Fig. 7 — Vickers microhardness profiles across the weldment formed in different conditions studied. Microhardness was measured in the direction indicated in the inset image.

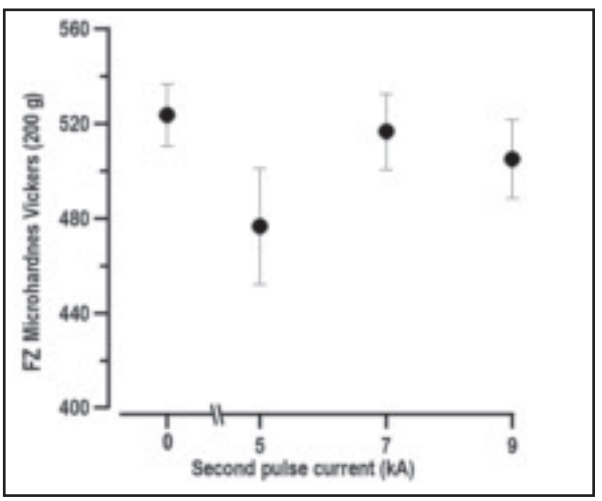

Fig. 8 — Variation of average FZ microhardness as a function of the second-pulse current applied during RSW of TRIP steel.

in the TPC 5-kA specimen during the second impulse current according to Fig. 3, thus suggesting tempering of martensite at this pulse condition.

The macrostructure of the TPC 7-kA specimen (Fig. 4C) shows significant differences in the weld nugget compared to the SPC condition. For example, the original periphery of the nugget that formed during the first pulse was barely visible after the second current impulse of TPC 7 kA. The elongated columnar grain growth (first impulse current) seemed transformed into an apparent quasi-equiaxed grain morphology (during second impulse current), which is confirmed in the FZ microstructure shown by Fig. 5C. These quasi-equiaxed grains contrast well with the elongated columnar grains oriented toward the weld nugget centerline of the SPC specimen — Fig. 5A. The above results indicate that at intermediate values of second impulse current (i.e., 7 kA), the grain morphology developed during the first impulse current is transformed into new grains upon the second impulse current, thus suggesting grain recrystallization. Peak temperature above Ac_3 (i.e., ~1150°C) is developed in TPC 7 kA during the second impulse current (i.e., re-austenitization), according to Fig. 3; thus, the peak temperature upon this condition is high enough for the elongated columnar grains (prior austenite grain boundaries) to recrystallize into quasi-equiaxed grains as a result of reaustenitization.

In the case of the TPC 9-kA specimen, a remelted nugget region was observed overlapped to the prior nugget of the first current impulse as depicted by Fig. 4D. The remelted nugget shape had a thinner appearance and new solidified macrostructure was revealed. The formation of the remelted nugget can be attributed to the higher current intensity of the second pulse cycle (9 kA). The resolidified structure in TPC 9-kA depicts coarser elongated columnar grains oriented toward the centerline of the nugget — Fig. 5D. It may be noted that the solidification structure is partially observed along with the postsolidification structure, which is comparable to that in the SPC specimens (Fig. 5A); however, the elongated columnar grains seemed coarser in the TPC 9-kA specimen.

The average weld nugget size measured in the metallographic cross-sectioned sample is plotted in Fig. 6 for the SPC as well as the second pulse current specimens. It can be seen that the weld nugget size was constant at about 6 mm for most of the specimens, except the specimen subjected to the second current pulse of 9 kA (TPC 9 kA) that had a slightly larger average nugget size. The increased nugget size in TPC 9 kA was a result of remelting during the second pulse current. The approximate weld nugget size can also be visualized from the macrographs illustrated in Fig. 4.

Hardness and Microstructure

Figure 7 delineates the Vickers microhardness profiles of TRIP steel subjected to different welding conditions obtained across the welded specimens from the center of the nugget (i.e., plotted at zero in the x axis) moving toward the base metal. The path of indentations followed AWS standard procedures (Ref. 16) as indicated by the inset image — Fig. 7. The microhardness of the base metal was found situated at a distance of about 5 mm from the center of the nugget with an average value of 255 ± 4 HV. The maximum hardness values in the profiles (i.e., 520 and 545 HV for TPC 9 kA and SPC, respectively) were found at the coarse grain region of the HAZ. It should be noted in Fig. 7 that the location of the maximum hardness for the TPC 9-kA specimen was shifted to the right, which is attributed to the extension of the FZ due to remelting of the nugget as shown in Fig. 4. Additionally, a number of indentations were performed at the center of the weld nugget in order to improve the accuracy of the measurements in that region and for further comparison

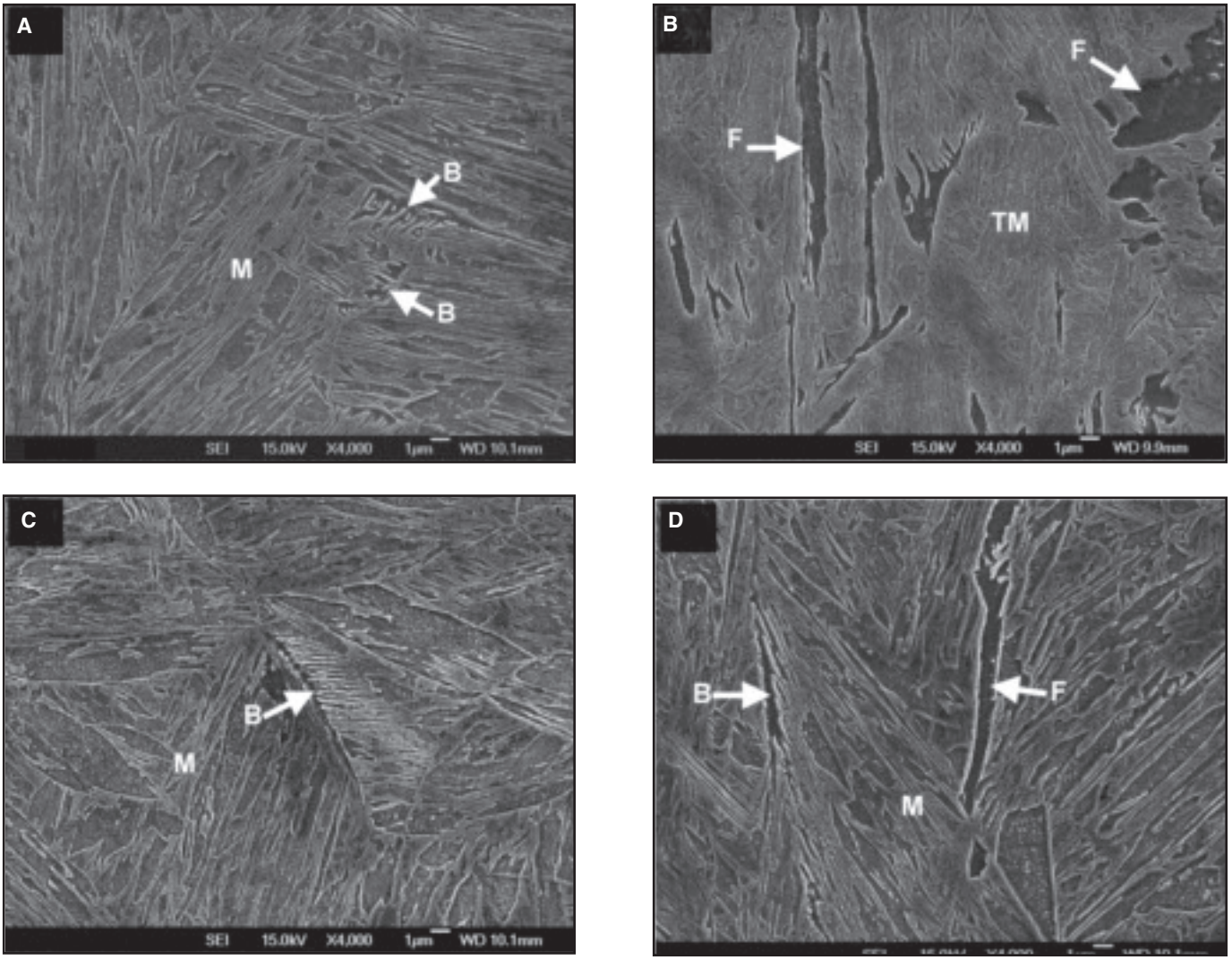

Fig. 9 — Representative SEM micrographs of the FZ in specimens subjected to the following: A —Single-pulse current, and second- pulse current at B — 5 kA; C — 7 kA; D — 9 kA.

with the FZ hardness of all the specimens — Fig. 8. The average FZ hardness of the TPC 5-kA specimen (i.e., 476 HV) was lower with respect to that of the SPC specimen (i.e., 523 HV). The TPC 7 kA resulted in FZ hardness (i.e., 516 HV) comparable to that of the SPC specimen, whereas slightly lower FZ hardness (i.e., 505 HV) was measured for the TPC 9-kA specimen.

The FZ microstructures of the SPC and TPC (5, 7, 9 kA) conditions are illustrated in the SEM micrographs in Fig. 9A, and 9B–D, respectively. Predominantly martensite (M) laths with possible low volume fraction of bainite (B) located along the grain boundaries was consistently observed in the SPC and TPC 7 and 9 kA, as indicated by the arrows (Fig. 9A and 9C, D). The observed bainite displayed a morphology similar to that of typical upper bainite (Ref. 21). In addition, formation of side-plate structures of ferrite (F) in the TPC 9-kA specimen is shown in Fig. 9D. On the other hand, the FZ microstructure of TPC 5-kA specimens revealed possible tempered martensite (TM) morphology along with considerable fraction of ferrite (F) in the form of elongated needle- and/or plate-like morphology as marked by the arrows — Fig. 9B. Tempering of martensite in TPC 5-kA specimen seemed consistent with a previous report on in-situ tempering of TRIP steels (Ref. 10).

The hardness values (Fig. 8) were observed to be in good agreement with the FZ microstructures (Fig. 9). For instance, comparable microhardness was observed for the SPC and TPC 7- and 9-kA specimens in which martensite was revealed as the predominant phase along with the presence of bainite. The further reduction in hardness in the case of the TPC 9-kA specimen might be associated with the presence of small volume fraction of side-plate structures of ferrite in the remelted structure — Fig. 9D. It is worth noting that very rapid cooling rates were developed in the FZ of all specimens (Fig. 3) owing to the hold time period in which the copper electrodes remained in contact with the steel sheet surfaces (Ref. 22), thus leading to formation of predominantly martensite. However, some differences might be pointed out among SPC and TPC 7- and 9-kA conditions. For example, the TPC 7-kA specimen achieved temperature well above the upper critical temperature Ac_3 (i.e., approximately 1100°C) upon the second pulse current (Fig. 3), thus any martensite formed after the first pulse retransformed to austenite during the second current pulse with formation of new grains (recrystallization). Rapid cooling rates were experienced after reaustenitization and, again, predominantly martensite was reformed along with bainite, at this point, SPC curves and TPC 7-kA curves seemed to develop similar cooling rates — Fig. 3. On the other hand, TPC 9-kA specimens reached temperatures well above the melting point (Fig. 3) upon the second current pulse, which resulted in remelting of the FZ formed after SPC, thus forming a new nugget with a thinner ap-

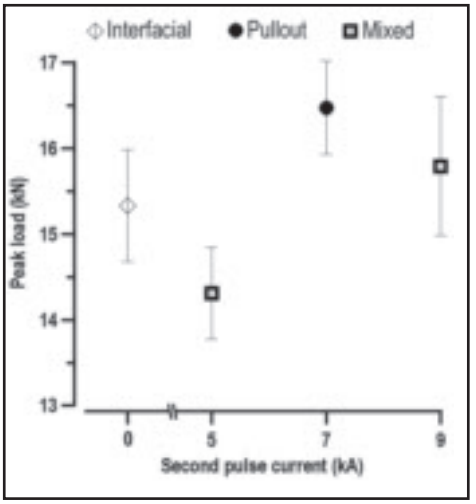

Fig. 10 — Maximum lap-shear tensile loads as a function of second-pulse current applied during RSW of TRIP steel.

pearance — Fig. 4. It is noteworthy that after remelting, the specimen was subjected to extended cooling times (Fig. 3) for transformation between Ac_3 until M_s temperatures compared to those in TPC 7-kA and SPC specimens, indicating slightly lower cooling rate. For example, Ms temperature upon cooling from Ac_3 was achieved after a period of more than 2 s (Fig. 3), thus experiencing the longest cooling time of all specimens. Thus, remelting of the nugget coupled with sufficient time between Ac_3 and M_s temperatures resulted in the formation of side-plate ferrite phase before reaching M_s temperature.

The reduction in FZ microhardness for the TPC 5-kA specimen was due to the presence of a larger fraction of side-plate ferrite and mainly to possible tempered martensite structure as illustrated in Fig. 9B. According to the simulated thermal history of the TPC 5-kA specimens in Fig. 3, the lowest temperature achieved by the FZ upon cooling, just before the second pulse current, was estimated to be 285°C, which is well below the M_s temperature (Table 2). An attempt to calculate the volume fraction of transformed martensite at 285°C was made by employing the Koistinen and Marburguer formulation (Ref. 23), suggesting ~72% of martensite in the FZ just before executing the second pulse. On the other hand, the maximum temperature achieved by the material upon the second pulse (~ 600°C) was below the lower critical temperature (Ac_1) (Table 2), thus indicating that in TPC 5-kA specimens, tempering of martensite microstructure could be possibly developed in the FZ in spite of the fact that the relatively high content of Si in the alloy retards the nucleation and growth of carbide precipitation (Refs. 24, 25). Furthermore, it is believed that small carbides are also contained within the tempered martensite regions (Ref. 26), which could not be resolved through SEM observations. The formation of ferrite plates can be associated with the presence of retained austenite from the first pulse cooling cycle, which further transformed, during second pulse, to form ferrite plates (Ref. 27). According to the Koistinen and Marburguer calculation, the microstructure just before reheating the FZ through the second pulse current was composed of approximately 28% retained austenite, which transformed into ferrite plates when reheated below Ac_1 (around 600°C) during the second pulse current. After the termination of the second pulse, any rapid cooling had no effect on the microstructural changes.

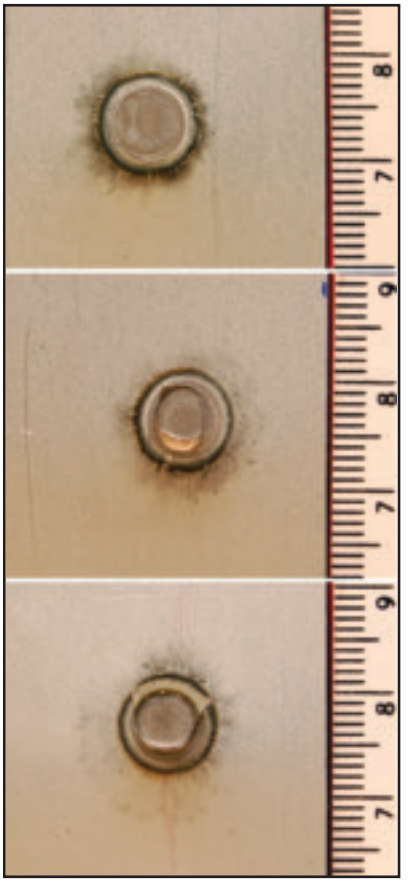

Fig. 11 — Representative lap-shear tensile failed specimens showing the following: A — Interfacial; B — partial interfacial; C — pullout failure modes.

Joint Tensile-Shear Performance

The average maximum lap-shear tensile load (failure) achieved in the specimens studied is plotted in Fig. 10 as a function of second pulse current. It is to be noted that the peak load of the SPC specimen corresponds to zero second pulse current of the graph and that of TPC specimens corresponds to 5-, 7-, and 9-kA second pulse current. Figure 11 illustrates representative fractured surfaces obtained after the lap-shear tensile test of all the specimens.

An averaged maximum load of about 15.3 ± 0.6 kN was obtained on the SPC specimens — Fig. 10. Interfacial failure (IF) mode was found in the entire batch of the SPC specimens investigated; the typical IF surface is delineated in Fig. 11A. The maximum failure load on TPC specimens varied according to the second pulse current level. For instance, an averaged maximum load of 14.3 ± 0.5 kN was obtained on TPC 5-kA specimens whereas increased maximum loads of 15.7 ± 0.8 and 16.4 ± 0.5 were found on the TPC 9- and 7-kA specimens, respectively. Two-pulse current 5-kA specimens resulted in a combination of two different failure modes (i.e., mixed); for instance, 50% of the tested specimens failed in IF mode and the remaining half of the batch in partial interfacial (PI) mode. A typical example of partial interfacial failure occurring in a TPC 5-kA specimen is shown in Fig. 11B. For the case of TPC 7-kA specimens, the failure mode was completely pullout (PO) in which the fracture was basically extended along the fusion boundary for all the assessed specimens with a fractured appearance depicted in Fig. 11C. Further increasing the current level of the second pulse (i.e., TPC- 9 kA) resulted in mixed failures with the following percentages: 33% as IF, 17% as PI, and the remaining in PO mode. The increased maximum load to failure for TPC 7 kA in comparison to the other conditions is attributable to consistent pullout failures observed in the full batch of assessed specimens. It is to be recalled from Fig. 6 that all the specimens resulted in comparable weld nugget size except slightly larger nugget size in TPC-9kA. Thus, it is conceivable to compare all the specimens with respect to their load-bearing capacity. Hence, it is concluded that the best lap-shear tensile performance, based on the peak load and failure mode, was achieved in the TPC 7-kA condition — Figs. 10, 11C. Interestingly, in spite of the slightly larger weld nugget size of the TPC 9-kA specimens (Fig. 6), the load-bearing capacity did not improve in comparison to that reached by the TPC 7- kA specimens.

The second impulse current condition strongly influenced on the failure mode of TRIP steel, which in fact is associated with the microstructural changes occurring in the weld nugget. For example, pullout failure in the TPC-7 kA specimen can be well attributed to formation of quasi-equiaxed grains of martensite in the weld nugget owing to reaustenitization during the second impulse current (i.e., 7 kA). In this regard, it is believed that the recrystallized grain morphology improved the weld toughness, thus impeding the possible

fracture path along the nugget centerline.

In summary, the lap-shear tensile performance of the second pulse current condition, except TPC 5 kA, seemed to improve based on the load-carrying capacity (higher peak loads) and pullout fracture mode due to microstructural changes. Among all assessed conditions in the present study, the optimal mechanical performance was achieved by the specimens subjected to two-pulse procedures with second pulse current of 7 kA. This is basically related to the postweld local heat treatment in which temperatures above Ac_3 was reached resulting in reaustenitization of the microstructure. During reaustenitization, grain recrystallization is expected to occur and change in the weld nugget toughness is achievable mainly at the FZ centerline where undesirable interfacial failures can be avoided.

Summary

The fusion zone (FZ) microstructure and the mechanical behavior of resistance spot welded TRIP steel was successfully modified by applying local postweld heat treatments by second pulse currents in resistance spot welding (RSW). The main results in this study are listed as follows:

1. Improved lap-shear tensile behavior such as pullout failure mode and increased maximum load to failure were achieved upon conditions of intermediate levels of second pulse current (i.e., 7 kA) attributed to formation of quasi-equiaxed grains (recrystallization) of predominantly martensite in the FZ through reaustenitization.

2. Tempering of martensite along with a fraction of elongated plate-like ferrite was observed at the lower levels of second pulse current (5 kA) coupled with a clear reduction in FZ hardness. However, no improvement was observed in the lap-shear tensile behavior.

3. At the higher levels of second pulse current (9 kA), remelting and formation of a new solidified elongated columnar structure of predominantly martensite microstructure was seen in the fusion zone. A fraction of side plate structures of ferrite was observed in the FZ owing to extended cooling time from peak temperature. The slight improvement in the mechanical performance was due to the increased size of the weld nugget during remelting.

Acknowledgments

The authors would like to acknowledge the funding from Auto21, one of the Networks of Centres of Excellence supported by the Canadian government, The Initiative for Automotive Manufacturing Innovation (IAMI) supported by the Ontario government, International Zinc Association (IZA), Belgium, Arcelor Mittal Dofasco, and Huys Industries in Canada. V. H. Baltazar Hernandez would also like to acknowledge the support from CONACYT Mexico and the Autonomous University of Zacatecas Mexico. The authors would like to acknowledge the comments and suggestions of Prof. Scott Lawson and Dr. Sashank Nayak from the Centre for Advanced Materials Joining at the University of Waterloo.

References

1. *Advanced High Strength Steel (AHSS) Application Guidelines.* 2009. Committee on Automotive Applications, International Iron and Steel Institute (eds.), Version 4.1, June, pp. 1–4.

2. Resistance Welding Manufacturing Alliance, *www.aws.org/rwma/.* Accessed November 8, 2009.

3. Baltazar Hernandez, V. H., Kuntz, M. L., Khan, M. I., and Zhou, Y. 2008. Influence of microstructure and weld size on the mechanical behaviour of dissimilar AHSS resistance spot welds. *Sci. Technol. Weld. Joining* 13(8): 769–776.

4. Khan, M. I., Kuntz, M. L., and Zhou, Y. 2008. Effects of weld microstructure on static and impact performance of resistance spot welded joints in advanced high strength steels. *Sci. Technol. Weld. Joining* 13(1): 49–59.

5. Smith, S., and den Uijl, N. 2006. Resistance spot welding of advanced high strength steels for the automotive industry. *The 4th International Seminar on Advances in Resistance Welding*. Wels, Austria, pp. 30–60.

6. Khan, M. I., Kuntz, M. L., Biro, E., and Zhou, Y. 2008. Microstructure and mechanical properties of resistance spot welded AHSS. *Mater. Trans.*, JIM, 49(7): 1629–1637.

7. Rathbun, R. W., Matlock, D. K., and Speer, J. G. 2003. Fatigue behavior of spot welded high-strength sheet steels. *Welding Journal* 82(8): 207-s to 218-s.

8. Jiang, C., Chiang, J., Zhao, J., and Zhou, Y. 2004. A new perspective on failure modes and weldability lobe of resistance spot welds of advanced high strength steels. AWS Sheet Metal Welding Conference XI, Sterling Heights, Mich. Paper 6-1.

9. *Resistance Welding Manual*, 4th Ed. 2003. Resistance Welding Manufacturing Alliance (RWMA). Miami, Fla.: American Welding Society.

10. Chuko, W. L., and Gould, J. E. 2002. Development of appropriate resistance spot welding practice for transformation-hardened steels. *Welding Journal* 81(1): 1-s to 7-s.

11. Peterson, W., and Gould, J. 2006. Development of spike temper diagrams for a range of advanced high strength steels. Sheet Metal Welding Conference XI, AWS Detroit Section, Detroit, Mich. Paper 6–4.

12. Hilditch, T. B., Speer, J. P., and Matlock, D. K. 2007. Effect of susceptibility to interfacial fracture on fatigue properties of spot-welded high strength steel. *Mater. Des.* 28: 2566–2576.

13. Xia, M., Tian, Z., Zhao, L., and Zhou, Y. 2008. Metallurgical and mechanical properties of fusion zone of TRIP steels in laser welding. *ISIJ Int.* 48-4: 483–488.

14. Yurioka, N., Suzuki, H., Ohshita, S., and Saito, S. 1983. Determination of necessary preheating temperature in steel welding. *Welding Journal* 62(6): 147–153.

15. Yurioka, N. Weldability calculation, *http://homepage3.nifty.com/yurioka/ exp.html*. Accessed on Nov. 11, 2009.

16. AWS D8.9/D8.9M: 2002, *Recommended Practices for Test Methods for Evaluating the Resistance Spot Welding Behavior of Automotive Sheet Steel Materials*. Miami, Fla.: American Welding Society.

17. Bramfitt, B. L., and Benscoter, A. O. 2002. *Metallographer's Guide: Practices and Procedures for Irons and Steels.* ASM International, 1st ed., p. 215.

18. Baltazar Hernandez, V. H., Panda, S. K., Okita, Y., and Zhou, Y. 2010. A study on heat affected zone softening in resistance spot welded dual phase steel by nanoindentation. *J. Mater. Sci.* 45: 1638–1647.

19. *www.rccm.co.jp/seihin/quickspot/index.html.* Accessed Oct. 2, 2009.

20. Kou, S. 2003. *Welding Metallurgy*. Wiley-Interscience, 2nd ed., p. 232.

21. Furuhara, T., Kawata, H., Morito, S., and Maki, T. 2006. Crystallography of upper bainite in Fe-Ni-C alloys. *Mater. Sci. Eng. A* 431: 228–236.

22. Baltazar Hernandez, V. H., Kuntz, M. L., and Zhou, Y. 2008. Fusion zone microstructures in resistance spot welding of TRIP to HSLA. AWS Sheet Metal Welding Conference XIII, Livonia, Mich. Paper 1-3.

23. Koistinen, D. P., and Marburguer, R. E. 1959. A general equation prescribing the extent of the austenite-martensite transformation in pure iron-carbon alloys and plain carbon steels. *Acta Metallurgica* 7: 59–60.

24. Speich, G. R., and Leslie, W. C. 1972. Tempering of steel. *Met. Trans.* 3: 1043.

25. Nayak, S. S., Anumolu, R., Misra, R. D. K., Kim, K. H., and Lee, D. L. 2008. Microstructure-hardness relationship in quenched and partitioned medium-carbon and high-carbon steels containing silicon. *Mat. Sc. Eng. A* 498: 442–456.

26. Pacyna, J., Jedrzejewska-Strach, A., and Strach, M. 1997. The effect of manganese and silicon on the kinetics of phase transformations during tempering — Continuous heating transformation (CHT) curves. *J. Mat. Proc. Tech.* 64: 311–318.

27. Online *ASM Handbook on Heat Treating*, Vol. 4. Accessed Dec. 14, 2009. *http://products.asminternational. org/hbk/index.jsp.*